Organic-Inorganic Halide Perovskite quasi-particles nature analysis via the interplay among classic solid state concepts, Density Functional, and Many Body Perturbation Theory

Jacky Even, Giacomo Giorgi, Claudine Katan, H. Kawai, Koichi Yamashita

To cite this version:

Jacky Even, Giacomo Giorgi, Claudine Katan, H. Kawai, Koichi Yamashita. Organic-Inorganic Halide Perovskite quasi-particles nature analysis via the interplay among classic solid state concepts, Density Functional, and Many Body Perturbation Theory. Giacomo Giorgi, Koichi Yamashita. Theoretical Modeling of Organohalide Perovskites for Photovoltaic Applications, CRC Press, 2017, 9781498750783. hal-01485462

HAL Id: hal-01485462
https://hal.science/hal-01485462

Submitted on 26 Jul 2021

Chapter 7: Organic-Inorganic Halide Perovskite quasi-particles nature analysis *via* the interplay among classic solid state concepts, Density Functional, and Many Body Perturbation Theory.

J. Even[1], G. Giorgi[2], C. Katan[3], H. Kawai[4], K. Yamashita[4]

[1]Insa de Rennes, Foton Laboratory UMR 6082, 20 avenue des Buttes de Coësmes, CS 70839,
35708 Rennes Cedex 7, France.
[2]Department of Civil and Environmental Engineering (DICA), The University of
Perugia, Via Goffredo Duranti 93, I-06125 Perugia, Italy.
[3]Institut des Sciences Chimiques de Rennes UMR 6226 Université de Rennes 1 Campus de
Beaulieu 35042 Rennes, France.
[4]Department of Chemical System Engineering, School of Engineering, The University of
Tokyo, 7-3-1, Hongo, Bunkyo-ku, Tokyo, Japan, and CREST-JST, 7 Gobancho, Chiyoda-ku,
Tokyo 102-0076, Japan

7. 1 Quasi particles behavior in 2D/3D organic-inorganic halide perovskites

7.1.1 Excitons

For the sake of clarity and coherence, this chapter devoted to the nature of quasi-particles in organic-inorganic halide perovskites will concentrate on lead-based perovskites. The exceptional light emission properties of layered hybrid organic-inorganic perovskite thin films or crystal structures are well documented in the literature over the last forty years (Ishihara et al. 1990, Koutselas et al. 1996, Mitzi et al. 1995). Intense light emission is indeed observed from helium to room temperature. Light absorption experiments have unambiguously revealed the excitonic character of the optical absorption at the electronic band gap edge. Extremely large exciton binding energies, ~300 meV (see Figure 7.1, (Ishihara et al. 1990)), have been measured as well as bound state resonances for the 1s up to 4s exciton states or for the biexciton and triexciton transitions (Even et al. 2012, Kato et al. 2003, Muljarov et al. 1995, Shimizu et al. 2006). Conversely, until recently little was known about excitons in 3D perovskites. The 50 meV binding energy recorded at 4 K in the early stages has only recently been shown to correspond to a large overestimation of the room temperature value (Even et al. 2014, Hirasawa et al. 1994).

The excitonic properties can be tailored mainly by two means: *(i)* by chemical engineering of the organic moiety and *(ii)* by changing the thickness of the inorganic layer. For instance, a series of layered 2D/3D structures of general formula $(R)_2(CH_3NH_3)_{n-1}Pb_nI_{3n+1}$, where R indicates a large size organic cation and n the number of lead iodide layers in the inorganic sheet, have been investigated experimentally for n=1-4. Noteworthy, the bulk 3D compound $CH_3NH_3PbI_3$ corresponds to $n=\infty$. Structural phase transitions of the layered hybrid crystal, which affect both the 2D inorganic lattice and the organic barrier, may lead to the switching of the exciton resonances and Peierls-like transitions. The energy shifts of the exciton lines are mostly related to distortions of the inorganic sublattice, *i.e*. rotations of the metal-halide octahedra that are coupled to ordering of the organic cations. These structural changes essentially renormalize the monoelectronic state energies without affecting much the oscillator strength of the optical transitions related to the bound exciton state. The situation is very different for 3D hybrid perovskites: structural phase transitions lead to both renormalization of the monoelectronic states and screening of the exciton resonances (Even et al. 2014).

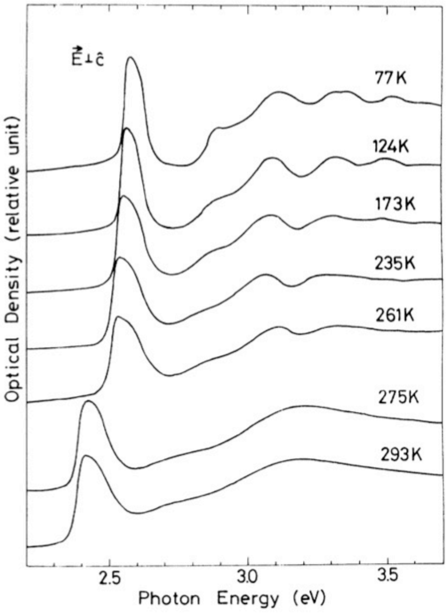

Figure 7.1

Optical density spectra in a cleaved thin crystal of $(C_{10}H_{21}NH_3)_2$ PbI_4 at several temperatures. Reprinted figure with permission from (Ishihara et al. 1990) Copyright (1990) by the American Physical Society.

Unfortunately, an accurate theoretical description of the monoelectronic states in layered hybrid perovskites crystals is involved. These materials are very large systems for atomistic approaches based on the density functional theory (DFT), which may face difficulties related to limited computational resources (Even et al. 2012, Even et al. 2014b). Furthermore, while numerous self-assembled hybrid perovskites have been studied as thin films, less crystallographic structures are known precisely. In fact, growth of monocrystals for X-ray or neutron diffraction may be difficult and the degradation of the lattice under irradiation or illumination can be a serious issue during experimental characterization. The flexibility of the molecules used to synthesize layered hybrid perovskite materials often promotes growth of self-assembled thin film, while introducing lattice disorder. For instance, with long alkyl chains, structural phase transitions with an order-disorder character have been reported at low temperature (Billing and Lemmerer 2007). For ordered structures having a reasonable number of atoms, *e.g.* $(pFC_6H_5C_2H_4NH_3)_2PbI_4$, $(C_5H_{11}NH_3)_2PbI_4$ or $(C_2H_4INH_3)_2PbI_4$, DFT computations are feasible (Even et al. 2012, Pedesseau et al. 2014). Moreover, it has been shown that a fast assessment of electronic properties and monoelectronic states, close to the band gap, can be achieved by replacing the molecular cation by a Cs^+ located at the position of the N atom. In most cases, this trick allows to mimic the ionic interactions due to the organic cations. Once spin-orbit coupling (SOC) is considered the DFT electronic structure reveals a direct band-gap character in agreement with the observed luminescence at room temperature (Even et al. 2012, Even et al. 2013). We stress that SOC plays a major role for the effective mass and degeneracy of the conduction band edge electronic state. But, DFT+SOC calculations underestimate the fundamental transition energy, as a result of an inherent limitation of DFT, which is a ground state theory. This limit can be overcome by implementing many-body effects, *e.g.* GW self-energy corrections for conduction and valence band states close to the band gap. Such calculations are already involved for crystals with smaller unit cells, namely 3D hybrid perovskites (Brivio et al., 2014, Even et al. 2014c, Umari et al. 2014), and are currently beyond available computational resources for layered hybrid perovskites. Meanwhile, the overall picture catch by DFT+SOC calculations on layered hybrids holds: they can be viewed as pure 2D systems with electronic states of specific symmetries. They provide detailed information on Bloch states and selection rules that can lead to further investigations using semi-empirical approaches (*e.g.* in **k.p** theory, tight-binding approximation) (Even et al. 2012, Even et al. 2014b). Such fundamental studies are important to understand the optical properties as well as the anisotropic electronic transport. Good in plane carrier transport allowed nice demonstration of thin-film transistors, but similar vertical transport has not yet been reported.

For layered hybrid perovskites, most of the experimental optical absorption spectra evidence very large exciton binding energies, in the 250-350meV range (see Figure 7.1). The enhanced exciton binding energy, as compared to that of 3D hybrid perovskites, is related to dielectric confinement and image-charge effects. These effects stem from the dielectric mismatch between the inorganic and organic layers. In layered hybrid perovskites, qualitative analyses of the excitons rely on the 2D Wannier exciton picture (Muljarov et al. 1995). It provides a reasonable account of experimental results and can be extended to understand the influence of halogen alloying. Unfortunately, unlike many of the conventional semiconductors, a quantitative analysis based on the Bethe-Salpeter equation (BSE) starting from monoelectronic states computed at the DFT+GW level is still beyond reach (Even et al. 2014c). Thus, alternative empirical approaches have been implemented to investigate the monoelectronic states and the enhancement of the exciton resonances due to dielectric confinement.

In the 1990's, David Mitzi introduced the quantum well (QW) concept that affords a schematic/qualitative picture: the layered HOP is approximated as being built from two bulk semiconductors A and B (similar to those sketched on Figure 7.2(a)), with inorganic sheets (A) alternating with organic layers (B) of much larger band gaps (Even et al. 2014b, Mitzi et al. 2001). However, this qualitative picture of a type-I QW-like heterostructure leads to inadequate analysis of quantum confinement, especially when it is combined with an effective mass approach. As a matter of fact, slowly varying envelope functions $F_i(r)$ are required to write the electronic wavefunctions of the heterostructure:

$$\psi(r) = \sum_i F_i(r) U_i(r) \qquad (7.1)$$

where $U_i(r)$ are periodic and rapidly oscillating basis functions. The Bloch functions of the bulk materials $U_{A,i}(r)$ and $U_{B,i}(r)$ are assumed to differ only slightly at high symmetry points of the Brillouin zone:

$$U_i(r) \approx U_{A,i}(r) \approx U_{B,i}(r) \qquad (7.2)$$

This condition is obviously not fulfilled in layered hybrid perovskites. Moreover, this fully empirical approach predicts a superlattice effect and a strong vertical electronic coupling that are neither confirmed by DFT, nor evidenced through carrier transport measurements. Alternatively, defining the whole layered hybrid perovskite as a composite material allows to quantitatively evaluated confinement potentials. It leads to a rigorous composite approach to afford the valence band-lineup between inorganic and organic layers (see Figure 7.2, (Even et al. 2014b)).

In order to analyze the confinement effect, the band gap of all-inorganic and hybrid perovskite colloidal slabs, as well as layered hybrid perovskites structures, can be written as a function of the number of layers *n*:

$$E_g(n) = E_{g;bulk} + \delta E_g(n) \qquad (7.3)$$

where $E_{g;bulk}$ is the band gap of the bulk core material (*e.g.* $CH_3NH_3PbX_3$, X=I, Br or Cl) and $\delta E_g(n)$ stems from quantum and dielectric confinement (Even et al. 2012, Sapori et al. 2016). Proper evaluation by DFT of the band gap, for instance $E_{g;bulk}$, requires the inclusion of self-energy corrections. For $CH_3NH_3PbI_3$several values of $E_{g;bulk}$ are available at the GW+SOC level.

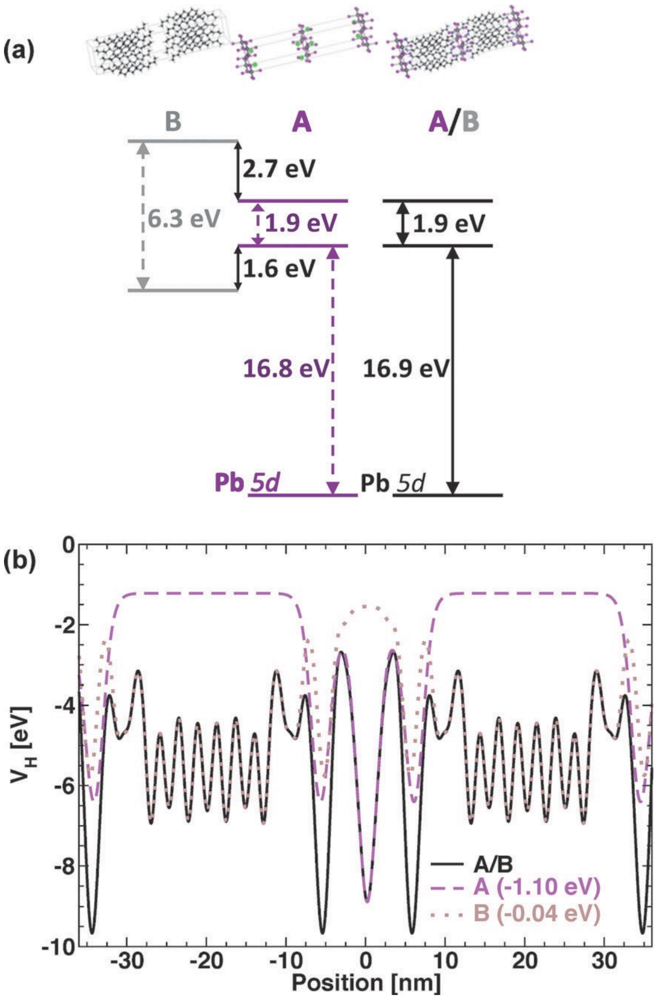

Figure 7.2.

a) Schematic representation of the CB and VB band alignment considering the $(C_{10}H_{21}NH_3)_2PbI_4$ layered hybrid perovskite (A/B) as a composite structure made of A and B modeled by $(Na)_2PbI_4$ and $C_{10}H_{21}CH_3$, respectively. b) Computed potential profiles for the real layered material (A/B, straight line) and A (dashed line) and B (dotted line) bulk-like materials. Band alignment and match of potential profiles of A/B are obtained thanks to downward shifts of the data computed for A and B amounting to 1.1 and 0.04 eV, respectively. Alignment of Pb 5*d* orbitals between A/B and A also require a 1.1 eV shift. Reprinted with permission from (Even et al. 2014b). Copyright 2014 John Wiley and Sons.

Noteworthy, room temperature contributions related to electron-phonon coupling and stochastic rotations of the organic cations are not yet included. The various contributions to the electronic band gap of colloidal or 2D/3D structures can be estimated from theoretical calculations by using the following decomposition:

$$E_g(n) \approx E_{g;DFT,bulk} + \delta E_{g,DFT}(n) + \Sigma_{bulk} + \delta\Sigma(n), \qquad (7.4)$$

where $E_{g;DFT,bulk}$ and Σ_{bulk} are the bulk band gap evaluated at the DFT level and self-energy corrections due to many-body effects, respectively. Whenever the band gap is not badly underestimated and effective masses of the bulk materials are accurately described by plain DFT, effect of quantum confinement can be estimated from $\delta E_{g,DFT}(n)$. As stated above, this contribution is not properly described by a purely empirical approach. The band gap and effective masses evaluated at the DFT level may strongly differ from their DFT+GW counterparts. Due to error cancellation, the DFT electronic band gap and effective massescomputed without SOC of $CH_3NH_3PbI_3$ are fortuitously in reasonable agreement with those obatinaed at the DFT+GW+SOC level. Thus, the $\delta E_{g,DFT}(n)$ calculated without SOC yields a first valuable estimate of quantum confinement (Figure 7.3).

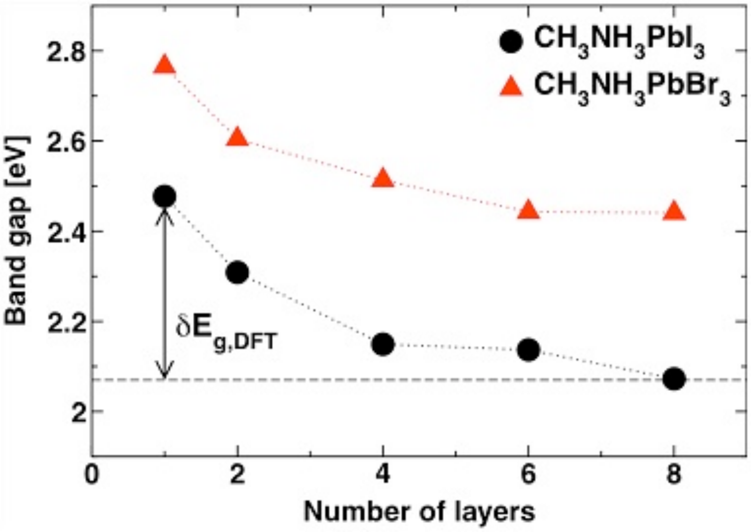

Figure 7.3:

Band gaps with respect to the slab thickness computed for slabs of $CH_3NH_3PbX_3$ (X = I, Br). Reproduced from (Sapori et al. 2016) with permission from The Royal Society of Chemistry.

Unfortunately, the variation of the self-energy with the number of layers, $\delta\Sigma(n)$, cannot be evaluated directly at the DFT+GW level due to non-affordable computational resources. An alternative is to use a semi classical evaluation of dielectric confinement on the monoelectronic states. In fact, purely classical analyses of the effect of dielectric confinement on the exciton resonances rely on a crude modeling of the dielectric profile through the heterostructure, namely an ad-hoc abrupt dielectric interface separating layers with bulk-like dielectric constants (Muljarov et al. 1995). This approach has several severe limitations. It leads to unphysical mathematical divergences of the self-energy profile $\delta\Sigma(z,n)$ at the interfaces (Muljarov et al. 1995, Sapori et al. 2016). It is also difficult to exactly define the size of the layers, as an atomistic description of the interfaces is lacking. Finally, often, the bulk dielectric constants of the bulk core materials $CH_3NH_3PbX_3$ itself is considered for the inorganic sheet, even for an ultrathin (n=1) inorganic layer. Using DFT to describe dielectric profiles of layered systems has been shown to improve accuracy, yet still at a reasonable computational cost (Sapori et al. 2016). This approach takes advantage of the *ab initio* description of the nanoplatelets or 2D/3D heterostructures and in particular of interfaces. It shows that in real 2D hybrid perovskites, a single standalone layer derived from the corresponding 3D $CH_3NH_3PbX_3$ material cannot solely approximate the inorganic layer. It allows accounting for various effects such as substitution of halide atoms, phonon contributions to the dielectric constant or comparison between all-inorganic and hybrid colloidal platelets. The dramatic effect of phonons especially shows off for the inorganic parts of the hybrid materials. The semi-classical evaluation of $\delta\Sigma(n)$, both for the CB and the VB states, can be obtained by computing the following integrals:

$$\delta\Sigma_{CB(VB)}(n) \approx \int \delta\Sigma(z,n)\rho_{CB(VB)}(z,n)dz \qquad (7.5)$$

where CB (VB) is the electronic density profile for the CB (VB) state. This value can be estimated at the center of the slab as shown in Figure 7.4.

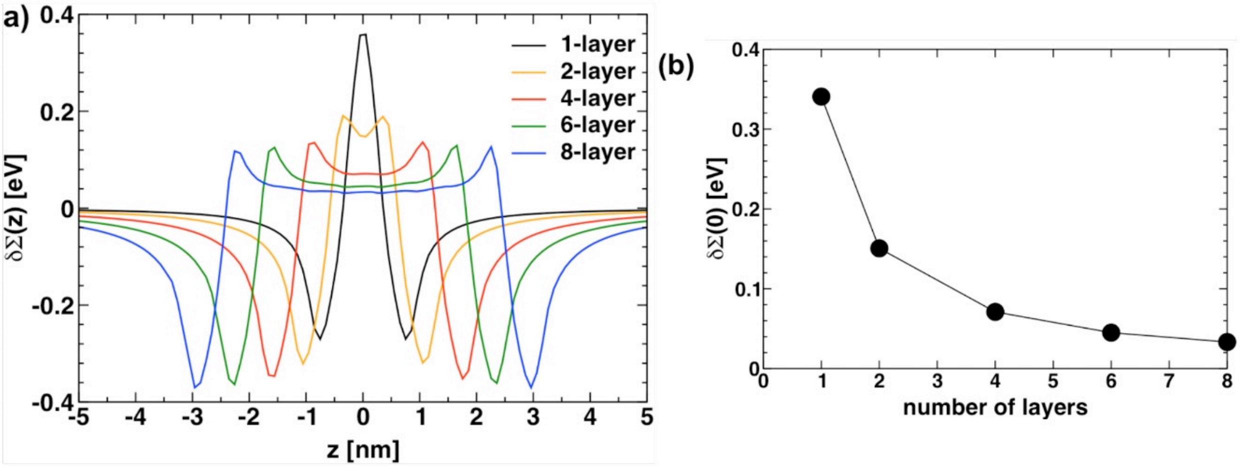

Figure 7.4.

(a) Self-energy profile δΣ(z) for slabs of $CH_3NH_3PbI_3$. (b) Self-energy taken at the slab center δΣ(0). Reproduced from (Sapori et al. 2016) with permission from The Royal Society of Chemistry.

We underline that it is not straightforward to identify the various contributions to the band gap that is actually derived from the optical absorption of colloidal or 2D/3D hybrid structures. Because the optical band gap corresponds to the electronic band gap minus the exciton binding energy, it undergoes a smoother variation than the band gap predicted using monoelectronic states. When the thickness decreases, the exciton binding energy increases and partially compensates the gap increase related to effects of quantum and dielectric confinement on the monoelectronic states.

At first approximation, the exciton binding energy $E_X(n)$ of all-inorganic and hybrid perovskite colloidal slabs, as well as layered hybrid perovskites structures, can be expressed in terms of the number of layers *n* as:

$$E_X(n) = E_{X,bulk}(n) + \delta E_X(n), \tag{7.6}$$

where $E_{X,bulk}(n)$ is the exciton binding energy of the bulk core material, *e.g.* $CH_3NH_3PbI_3$, and $\delta E_X(n)$ stems from quantum and dielectric confinement. $E_{X,bulk}(n)$ is an important parameter for photovoltaic devices operating at room temperature, especially for the ratio of free carrier to exciton populations. It is expected to strongly affect the charge transport through the structures. Besides, a careful reassessment of old experimental absorption spectra of $CH_3NH_3PbI_3$ revealed the importance of exciton screening at high temperature. In fact, simulation of the optical absorption spectra using an expression accounting both for bound and continuum pair states clearly evidences that the generally accepted value for $CH_3NH_3PbI_3$ (~50 meV, measured at 4 K (Hirasawa et al. 1994)) is inappropriate for describing the real exciton resonance at room temperature as shown in Figure 7.5 (Even et al. 2014, Ishihara 1994).

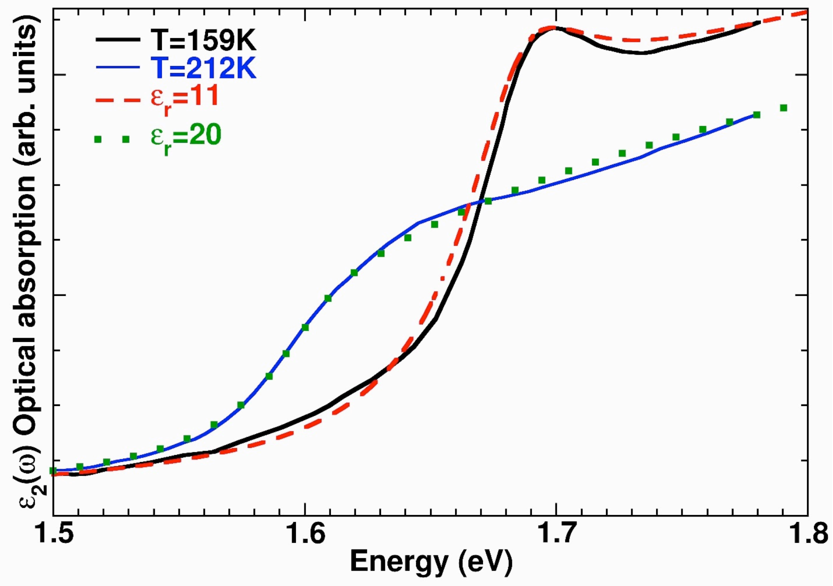

Figure 7.5.

Optical absorption spectra of $CH_3NH_3PbI_3$ highlighting exciton screening. Experimental data taken from (Kato et al. 2003) recorded at 159 K (black line) and 212 K (blue line) and computed spectra for bound and continuum pair states, considering two-particle wave function and effective mass equations for electron and hole. The effect of dielectric screening is shown for ε_{eff} =11 (red dash line) and 20 (green dot line) and leads to a good fit of the experimental spectra below (159K) and above Tc (212K), respectively. Reprinted with permission from (Even et al. 2014). Copyright 2014 American Chemical Society.

Excitonic effects in 3D hybrid perovskites can be accounted for using BSE starting from the monoelectronic states calculated at the DFT level. For instance, when taking the pseudo-cubic high temperature reference phase of $CH_3NH_3PbI_3$, enhancement of absorption at the bandgap can clearly be evidenced (Figure 7.6, (Even et al. 2014c)). Noteworthy, in the perturbative BSE/DFT approach, screening of the electron-hole interaction due to atomic motion is not taken into account. Thus, such a description is more suited to low temperature phases where these motions are expected to be frozen.

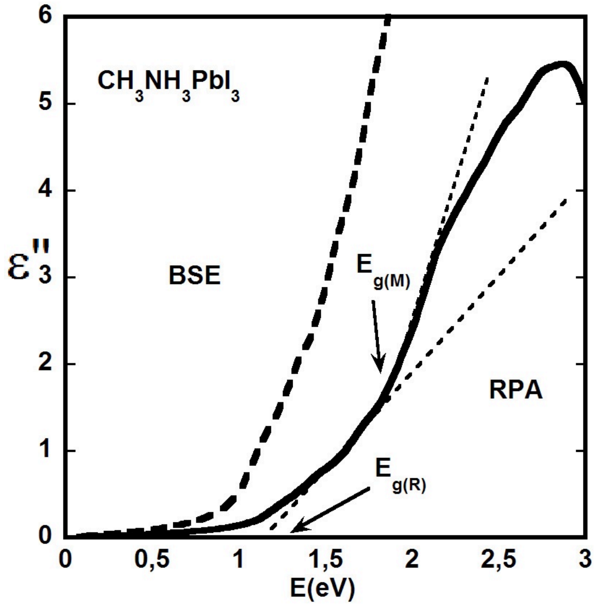

Figure 7.6.

Comparison of the dielectric constant variation of $CH_3NH_3PbI_3$ in the cubic phase with (dotted line, DFT+BSE calculation) and without (straight line, DFT+RPA calculation) the excitonic interaction. Onsets of optical transitions at *R* and *M* points of the Brillouin zone are indicated. Reprinted with permission from (Even et al. 2014c). Copyright 2014 John Wiley and Sons.

The discrepancy with high temperature experimental results stems from additional exciton screening, related to interactions between electrons and polar phonons, leading to an increased effective dielectric constant. Analysis of the structural phase transition of $CH_3NH_3PbI_3$ near 160K, further shows that besides a renormalization of the optical band gap related to distortion of the inorganic lattice, the thermally activated disorder of the polar cation's orientations associated to the phase transition may further screen the excitonic interaction (Even et al. 2014). Multiple exciton lines in the 25-75K temperature range have also been evidenced on a single crystal (Fang et al., 2015). The helium temperature exciton line was attributed to a bound exciton with a long lifetime, possibly arising from a strong coupling with the organic cations.

In the available literature, $\delta E_X(n)$ is mainly attributed to dielectric confinement effects. In a pioneer contribution, Muljarov et *al.* calculated the binding energies of excitons in layered hybrid perovskites (Muljarov et al. 1995). Their method, based on a classical resolution of BSE, was able to account for dielectric superlattice effects but, unfortunately, it relied on parameters fitted to experimental data. Moreover, to avoid unphysical divergences related to abrupt dielectric interfaces, a transitional layer at the interface between organic and inorganic parts had to be considered. Considering a more realistic dielectric profiles affords significant improvement for evaluating $\delta E_X(n)$. In fact, both monoelectronic and excitonic pair states should be treated at the same level of theory. Currently, semi-classical estimates of both $\delta\Sigma(n)$ and $\delta E_X(n)$ can be afforded based on a preliminary step where the dielectric profiles of colloidal nanoplatelets or 2D/3D hybrid perovskite are computed using DFT.

7. 1.2 Electron-Phonon Interactions

Electron-phonon coupling is well known to influence relaxation and broadening mechanisms as well as carrier transport and optical properties. Carrier scattering processes can be investigated in the weak coupling regime assuming independent particles and the scattering probabilities can be computed using the Fermi Golden rule. Group theory allows inferring corresponding selection rules and symmetry allowed couplings (Even 2015, Even et al. 2016). For the reference *Pm-3m* cubic space group of hybrid perovskites, the possible intravalley deformation couplings are summarized Table 7.1. None of the VBM and CBM states can couple to optical phonons via a zero order deformation potential (zero order ODP). Next, acoustic phonons and electrons can also interact via a deformation potential, but the coupling always vanishes at zero order. Due to SOC, only local volumetric strain (Γ_1^+) is expected to couple to VBM and CBM states and influence the first order acoustic deformation potential (ADP). Molecular degrees of freedom, which can be streamlined based on the concept of pseudo-spins (PS), may also yield an additional deformation potential mechanism for electrons in hybrid perovskites via elastic PS (EPS), similarly to deformation potential for phonons. The dynamical/stochastic configurations of elastic multipoles can show up along different scenarios (Table 7.1, (Even 2015, Even et al. 2016)). All of them can induce crystal potential fluctuations that can change the electron density. Regarding polar couplings of charge carrier, piezo-electric electron-phonon coupling (PZA) vanishes as a result of vanishing piezoelectric tensor components in *Pm-3m* crystal structures. The Frölich interaction between the delocalized CBM and VBM states and polar optical phonons (FOP) is most probably the dominant scattering process in $CH_3NH_3PbI_3$ as a result of dielectric increment between the high and medium frequency ranges related to Γ_4^- longitudinal optical modes. Dynamical and static disordered configurations of the molecular cations may induce additional Polar PS (PPS) excitations, which can couple to the charge carrier depending on the strength of the molecular electric dipole and the size of the polar domains.

Next, in standard semiconductors, one of the most relevant mechanisms of intraband hot-carrier relaxation is thermalization coupled with lattice vibrations. As the *slow hot-hole cooling* process is currently among the most controversial and debated feature of 3D $CH_3NH_3PbI_3$ (Xing et al. 2013), we discuss this process in more details. The UV–vis absorbance spectrum analysis shows two main absorption peaks: one at 760 nm and another at 480 nm; this latter is characterized by an impressively long lifetime (~0.4 ps), possible fingerprint of the mentioned slow hot-hole cooling in the valence band (VB).

	VBM R_1^+ SOC=0	VBM R_6^+ SOC≠0	CBM R_4^- SOC=0	CBM R_6^- SOC≠0
Strain Γ_1^+	✖	✖	✖	✖
Strain Γ_3^+	-	-	✖	-
Strain Γ_5^+	-	-	✖	-
Optical Phonons	-	-	-	-
Organic Cation Elastic PS (**A**)	✖	✖	✖	✖
Organic Cation Elastic PS (**B**)	✖	✖	✖	✖
Organic Cation Elastic PS (**C**)	✖	✖	✖	✖

Table 7.1. Possible intravalley deformation couplings in the reference *Pm-3m* cubic phase of hybrid perovskites. Crosses indicate couplings between CBM and VBM band edge electronic states at the *R* point of the *Pm-3m* Brillouin zone, and acoustic phonons (first order ADP, strains), optical phonons (zero order ODP) or elastic pseudospin (PS) at *Γ* point. Elastic PS are defined for the three scenarios **A**, **B** and **C** where the molecular axe points towards a cubic cell facet, an

halogen atom, or the center of an octahedron, respectively (Even 2015, Even et al. 2016).

In details, while the peak at 760 nm is undoubtedly associated with the valence band maximum (VBM) → conduction band minimum (CBM) direct excitation, the attribution of the peak at 480 nm still remains unclear. The results of Xing (Xing et al. 2013) show that the two states are composed of different VB states but same CB state, assigning the 480 nm peak to the transition from a band situated ~1 eV below VBM (VB2) to the CBM. To complete the scenario, early theoretical studies by some of us (Even et al. 2014) have suggested the state at 480 nm as composed of multibandgap absorption not only VB2 → CBM. There is thus still need to make the process clear and give accordingly a conclusive attribution to the 480 nm peak state.

Full first-principles calculations on electron-phonon interactions (*e-ph*) interactions, i.e., one of the most relevant mechanisms of intraband hot-carrier relaxation, have been introduced combining density-functional theory (DFT), density-functional perturbation theory (DFPT), and many-body perturbation theory (MBPT) (Cannuccia and Marini 2011, Kawai et al. 2014, Marini 2008). According to such scheme, $CH_3NH_3PbI_3$ and $CsPbI_3$, and also the charged semiconductor network, PbI_3^- (Giorgi et al. 2014) have been here analysed.

Concerning the theoretical details of the MBPT, in the coupled electron–nuclei system, the Hamiltonian, $\hat{H}$, is constituted by three components where $\hat{H}_0$ represents the electronic Hamiltonian corresponding to the case where the atoms are frozen at their equilibrium position, $\mathbf{R}_0$, while $\hat{H}_1$ and $\hat{H}_2$ are the first and second terms of the Taylor expansion of $\hat{H}_0$ with the atomic positions $\{\mathbf{R}\}$, respectively. In the present DFT based analysis, the electron–electron correlations were treated at the mean field level. $\hat{H}_0$ is approximated to Kohn-Sham (KS) Hamiltonian

$\hat{H}_0 \approx \sum_j [\hat{h}(\boldsymbol{r}_j)]$with $\hat{h}(\boldsymbol{r}_j) = -\frac{1}{2}\frac{\partial^2}{\partial \boldsymbol{r}^2} + \hat{V}_{scf}(\boldsymbol{r},\boldsymbol{R})\big|_{R=R0}$, where the electronic effective potential, $\hat{V}_{scf}$ is defined as $\hat{V}_{scf} = \hat{V}_{ion} + \hat{V}_{Hartree} + \hat{V}_{XC}$. MBPT enables us to calculate the two self-energies, the "Fan", $\Sigma_{i\mathbf{k}}^{\mathrm{Fan}}(\omega,T)$, and the "Debye-Waller (DW)", $\Sigma_{i\mathbf{k}}^{\mathrm{DW}}(T)$, associated with $\hat{H}_1$ and $\hat{H}_2$, respectively (Cannuccia and Marini 2013). The quasiparticle (QP) energy of the i^{th} band at the point $\boldsymbol{k}$ in the Brillouin zone, $E_{n\mathbf{k}}(T)$, that derives from such self-energies is

$$E_{ik}(T) = \varepsilon_{ik}^{KS} + Z_{ik}(T)[\sum\nolimits_{ik}^{Fan}(\varepsilon_{ik}^{KS},T) + \sum\nolimits_{ik}^{DW}(T) \qquad (7.7)$$

with $Z_{i\mathbf{k}}(T) = (1 - ((\partial\Sigma_{i\mathbf{k}}^{\mathrm{Fan}}(\omega,T))/\partial\omega)|_{\omega=\varepsilon_{i\mathbf{k}}^{\mathrm{KS}}})^{-1}$ representing the renormalization factor and $\varepsilon_{i\mathbf{k}}^{\mathrm{KS}}$ the KS energy of the electronic state at (i', $\mathbf{k}$–$\mathbf{q}$). The lifetime of the QP, $\tau_{i\mathbf{k}}(T)$, is related to the imaginary part of QP energy. Since the $\sum_{ik}^{DW}(T)$ is real, only the $\Sigma_{i\mathbf{k}}^{\mathrm{Fan}}(\omega,T)$ determines $\tau_{i\mathbf{k}}(T)$, . $\Sigma_{i\mathbf{k}}^{\mathrm{Fan}}(\omega,T)$ is represented as follows.

$$\sum\nolimits_{ik}^{Fan}(\omega,T) = \sum_{i',q\lambda} \frac{\left|g_{ii'\mathbf{k}}^{q\lambda}\right|^2}{N_q}\left[\frac{N_{q\lambda}(T)+1-f_{i'k\text{-}q}}{\omega-\varepsilon_{i'k\text{-}q}^{KS}-\omega_{q\lambda}-i0^+} + \frac{N_{q\lambda}(T)-f_{i'k\text{-}q}}{\omega-\varepsilon_{i'k\text{-}q}^{KS}-\omega_{q\lambda}-i0^+}\right] \qquad (7.8)$$

In eq. (7.8) $\omega_{\mathbf{q}\lambda}$ represents the phonon energy relative to the mode λ and the transferred momentum $\mathbf{q}$. The term $N_{\mathbf{q}\lambda}(T)$ is the Bose–Einstein distribution function of the phonon mode (λ, $\mathbf{q}$) at temperature T, and $f_{i'\mathbf{k}-\mathbf{q}}$ is the occupation number of the bare electronic state at (i', $\mathbf{k}$–$\mathbf{q}$). $N_{\mathbf{q}}$ is the number of $\mathbf{q}$-point in the simulation and 0^+ is a damping parameter. $g_{ii'k}^{\mathbf{q}\lambda}$ is the *e-ph* coupling matrix element defined as

$$g_{ii'\mathbf{k}}^{q\lambda} = \sum_{scf}(2M_s\omega_{q\lambda})^{-1/2}e^{iqr_i}\langle \boldsymbol{ik}|\frac{\partial\hat{V}_{scf}(\boldsymbol{r},\boldsymbol{R})}{\partial\boldsymbol{R}_{scf}}|i'\boldsymbol{k}-\boldsymbol{q}\rangle\xi_\alpha(\boldsymbol{q}\lambda\,|\,s) \qquad (7.9)$$

with M_s representing the mass of the atom occupying the τ_s position in the unit cell. The phonon polarization vectors are represented by the term $\xi_\alpha(\mathbf{q}\lambda|s)$. Phonons and the derivatives of $\hat{V}_{\mathrm{scf}}$ in eq.

(7.9) were calculated using DFPT. According to the on-mass-shell approximation, (i.e., $Z_{i\mathbf{k}}(T) = 1$ in eq. (7.7)) that we initially adopted, and focus on the case at $T = 0$ K, then $\tau_{n\mathbf{k}}$ is

$$\tau_{\mathrm{ik}}(T = 0K) = \left[\frac{2}{N_q} \sum_{i'q\lambda} \left| g_{ii'k}^{q\lambda} \right|^2 \delta\left(\varepsilon_{ik}^{KS} - \varepsilon_{i'k-q}^{KS} \pm \omega_{q\lambda} \right) \right]^{-1} \qquad (7.10)$$

where an upper (lower) sign of $\omega_{\mathbf{q}\lambda}$ is assigned when a state i' belongs to valence (conduction) band.

The optimized structures (Giannozzi et al. 2009, Kawai et al. 2015) of the $CH_3NH_3PbI_3$, $CsPbI_3$, and PbI_3^- systems are shown in Figure 7.7 with $CH_3NH_3PbI_3$, at variance with $CsPbI_3$ and PbI_3^-, showing a noticeable distorted structure from the ideal cubic one. The volume of the semiconductor network PbI_3^- increases with respect to the case of $CH_3NH_3PbI_3$ due to the absence of the attractive Coulomb interactions between aminic hydrogen and iodine atoms (Giorgi et al. 2014, Mosconi et al. 2013).

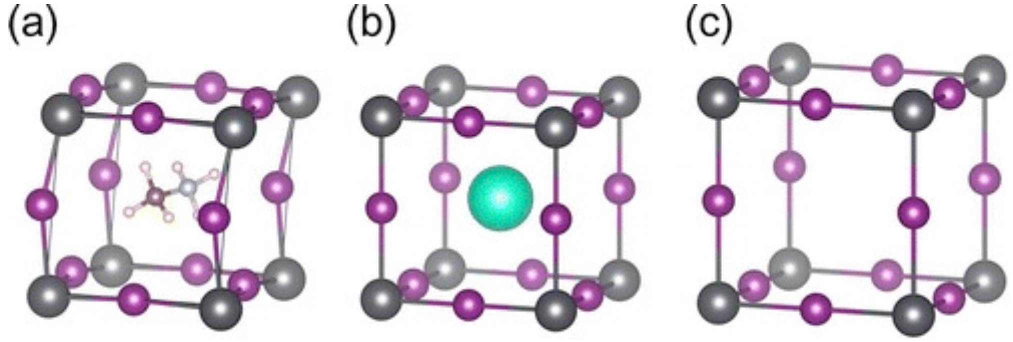

Figure 7.7.

Optimized structures of (a) $CH_3NH_3PbI_3$, (b) $CsPbI_3$, and (c) PbI_3^-. Large and small atoms in the network represent Pb and I, respectively. Inside the network (a) dark (light) larger atoms are C (N) while small white are H, respectively. In (b) the large atom inside the cage is Cs. Reprinted with permission from (Kawai et al. 2015). Copyright 2015 American Chemical Society.

From the DOS analysis, shown in Figure 7.8, the edges of both $CH_3NH_3PbI_3$ and $CsPbI_3$ are characterized by large band dispersions, resulting in light effective masses of both the electrons and holes, confirming the ambipolar nature of $CH_3NH_3PbI_3$ (Xing et al. 2013).

PbI_3^- whose DOS are reported in Figure 7.8(c) shows, at variance with the two previous cases, a reduced dispersion in the VBM, induced by the absence of the methylammonium group (reduction of the Pb 6*s* and I 5*p* orbital antibonding interaction (Giorgi et al. 2014, Huang and Lambrecht 2013). Accordingly, the DOSs in the VBM region of $CH_3NH_3PbI_3$ and $CsPbI_3$ will result smooth, while that of PbI_3^- shows a noticeably high peak. We will see below how this difference has a marked impact on the carrier lifetimes.

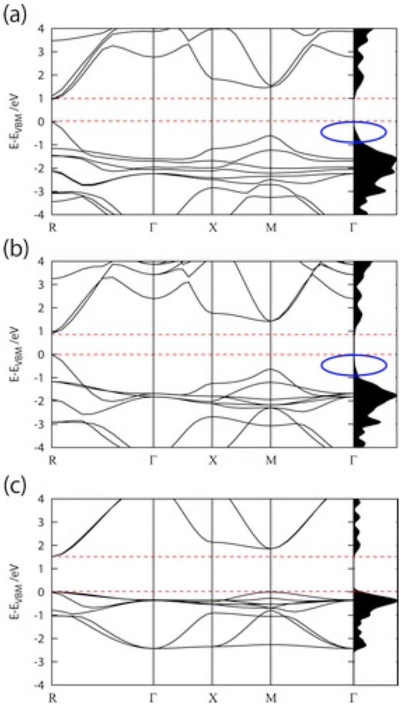

Figure 7.8.

Band plots (left) and DOS (right) of (a) $CH_3NH_3PbI_3$, (b) $CsPbI_3$, and (c) PbI_3^-. The red dotted lines show the VBM and CBM. [$\Gamma = (0, 0, 0)$, $X = (0.5, 0, 0)$, $M = (0.5, 0.5, 0)$, and $R = (0.5, 0.5, 0.5)$ in units of $2\pi/a$]. Reprinted with permission from (Kawai et al. 2015). Copyright 2015 American Chemical Society.

The phonons and *e-ph* coupling matrix (eq 7.10) were calculated using the DFPT scheme by PHonon code in the Quantum ESPRESSO. (Giannozzi et al. 2009) For both $CsPbI_3$ and $CH_3NH_3PbI_3$ we have considered the cubic polymorph, because of the computational burden associated to the large size of the room temperature stable polymorph which is orthorhombic for $CsPbI_3$ (*o*-$CsPbI_3$, *Pnma*, *Z*=4, 20 atoms) and tetragonal for $CH_3NH_3PbI_3$ (*t*-$CH_3NH_3PbI_3$, *I*4*cm*, *Z*=4, 48 atoms). In this way we can also compare systems with similar properties but with the drawback that the metastable cubic structures result in some imaginary phonon modes for the three species under analysis.

The resulting phonon bands are shown in Figure. 7.9 for the case of $CH_3NH_3PbI_3$. Notably, imaginary modes do not affect the mechanism of slow hot-hole cooling and the carrier lifetimes. In details, the phonon bands whose wavenumbers are higher than 200 cm^{-1} refer to methylammonium vibration. These contributions are decoupled from those with lower wavenumber associated with the lead iodide semiconductor network (Papavassiliou 1997), thus the band dispersion is not remarkable. To better observe the character of phonons with low wavenumbers, such region is indicated by an arrow in Figure 7.9(a) and magnified in Figure 7.9(b).

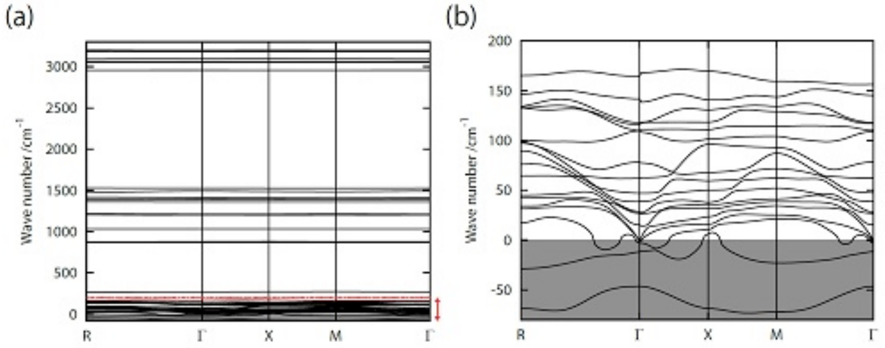

Figure 7.9. (a) Phonon band of $CH_3NH_3PbI_3$. Imaginary modes are represented as negative values in the shaded areas. (b) The phonon band in low wavenumber region indicated by an arrow in (a). Reprinted with permission from (Kawai et al. 2015). Copyright 2015 American Chemical Society.

The lifetimes *τ* calculated with and without the imaginary modes are plotted in Figure 7.10 along with the KS energies.$^{(a)}$ The fact that only the optical phonon modes strongly couples with the VBs makes the impact of these imaginary modes marginal in the three investigated systems.

Figure 7.10 also reveals that the τ in the VB of $CH_3NH_3PbI_3$ ($CsPbI_3$) begins to increase at $E–E_{VBM}$ ~ −0.3 eV ($E–E_{VBM}$ ~ −0.6 eV) (long lifetime region). Because of the enhancement in the lifetime, the relaxation of the hot holes in the two perovskites, the organic-inorganic and the fully inorganic, will be suppressed in the range $E–E_{VBM}$ between −0.3 and −0.6 eV, confirming the available experimental results for $CH_3NH_3PbI_3$ (Xing et al. 2013).

$^{(a)}$*MBPT calculations performed to obtain the self-energies and the lifetimes are performed with the Yambo code* (Marini et al. 2009). *For further details see* (Kawai et al. 2015).

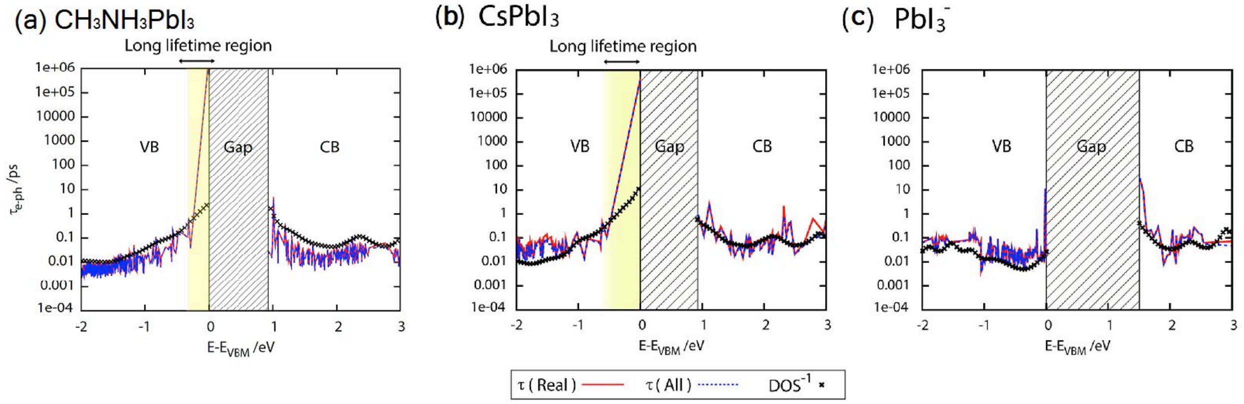

Figure 7.10.

Hot-carrier lifetimes of (a) $CH_3NH_3PbI_3$, (b) $CsPbI_3$, and (c) PbI_3^-. The blue (red) dotted lines are lifetimes with (without) the imaginary modes. Black crosses are the inverse of the DOSs shown in Figure 7.8. Partially adapted with permission from (Kawai et al. 2015). Copyright 2015 American Chemical Society.

In Figure7.10 the inverse of the DOSs are also plotted, showing the general correlation between the lifetime and the DOSs: in particular, the lifetime increases as the DOS becomes smaller

(Bernardi et al. 2014, Lautenschlager et al. 1986, Restrepo et al. 2009), and smaller DOS offers a reduced number of carrier relaxation paths leading to longer carrier lifetimes and vice versa. As a result, the long-lifetime region in both the organic-inorganic mixed perovskite and the fully inorganic one can be attributed to the small DOS region shown in Figure 7.8, long-lifetime that still from Figure 7.8 is absent in the case of the charged semiconductor network, PbI_3^-. Accordingly, we clearly predict that the slow hot-hole cooling is universally observed in $APbI_3$, as long as the characteristic small DOS is presented in their VBs. Figure 7.11(a) and 7.11(b) show the generalized Eliashberg functions of the two valence states A and B shown in the inset band plot. The analysis of such functions is extremely useful to explain the contribution of phonons to the carrier relaxation for each electronic state. Figure 7.11(a) clearly confirms that only phonon modes in low wavenumber range below 200 cm^{-1} have dominant contribution.

Similarly as in Figure 7.9, the low wavenumber region is indicated by an arrow in Figure 7.11(a) and magnified in Figure 7.11(b). In state A, the highest peaks (c) were in the range from 110 to 120 cm^{-1}. In state B, on the other hand, the highest peaks (d) were in the range from 140 to 170 cm^{-1}. The representative atomic motions in these peaks are shown in Figure 7.11(c) and 7.11(d). In both phonon modes, methylammonium vibrations are due to the light atomic masses of H, C, and N. However, the Pb-I network is similarly active. The difference between mode (c) and (d) is the motion of lead: it is indeed active in mode (c) but inactive in mode (d). This trend indicates that the carrier relaxation on the electronic state A is governed by motions of both Pb and I while the relaxation on the state B is governed by only I motion. This difference stems from the fact that state A is associated with the antibonding coupling between the Pb 6*s* and I 5*p* orbitals, but state B is mainly composed of I 5*p* orbital. This result is exactly the same as $CsPbI_3$ (Kawai et al. 2015).

In Figure 7.11(b), peak (e) is similarly indicated showing low contribution in both state A and B.

The atomic motion of this peak is also shown in Figure 7.11(e). In this mode, only the part of methylammonium is active. The negligible contribution from this mode is because the part of PbI_3 is inactive. Our analysis revealed that the hot carrier relaxation is independent by the vibration of methylammonium as hypothesized in our previous work (Kawai et al. 2015).

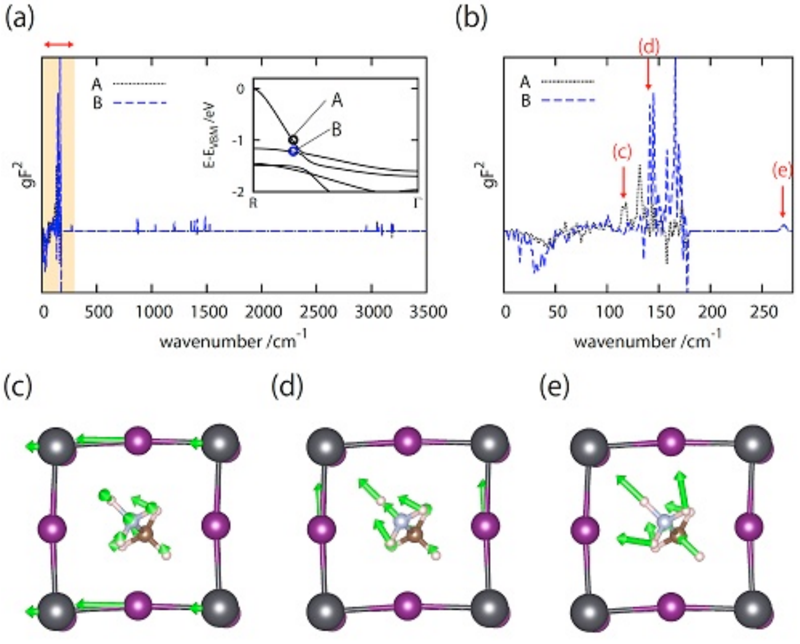

Figure 7.11.

(a) Generalized Eliashberg functions of $CH_3NH_3PbI_3$ for the two valence states A and B. Their positions are indicated in the inset band plot. (b) Generalized Eliashberg functions in small wave number region indicated by an arrow in (a). (c), (d), (e) Atomic motions of the phonon modes for (λ, $\mathbf{q}$) = (14, (0.5, 0.5, 0)), (λ, $\mathbf{q}$) = (17, (0.5, 0.5, 0)), (λ, $\mathbf{q}$) = (19, (0.5, 0.5, 0)) respectively. As in Figure 7.7. large and small atoms in the network represent Pb and I, respectively. Inside the network dark (light) larger atoms are C (N) while small white are H, respectively.

7.1.3 Electron-Electron Interactions

The effect of electron-electron (*e-e*) interactions on the optoelectronic properties of hybrid perovskites has been little explored experimentally. Here we proceed considering concepts already well developed for standard semiconductors (Haug and Koch, 2009). First we explore how large densities of free carriers can influence excitonic resonance and material gain. For instance, this may be important in photovoltaic cells under concentrated light or in laser structures with large carrier injection. To this end, the optical susceptibility can be written in terms of the exciton Green's function that can be obtained using BSE. But, a full DFT+GW+BSE treatment, which would allow accounting for non-linear effects induced by a free carrier population, is currently beyond available computational resources. To analyze the modifications of the optical spectrum close to the band gap, empirical models remain a good alternative. For instance, an empirical basis of electron and hole monoelectronic states obtained with the **k.p** method can prove efficient. This is illustrated Figure 7.12. In the linear regime, the BSE contains the dipole of the *e-h* optical transition at *R* as a source term and an *e-h* Coulomb interaction, which singularity deserves a specific numerical procedure.

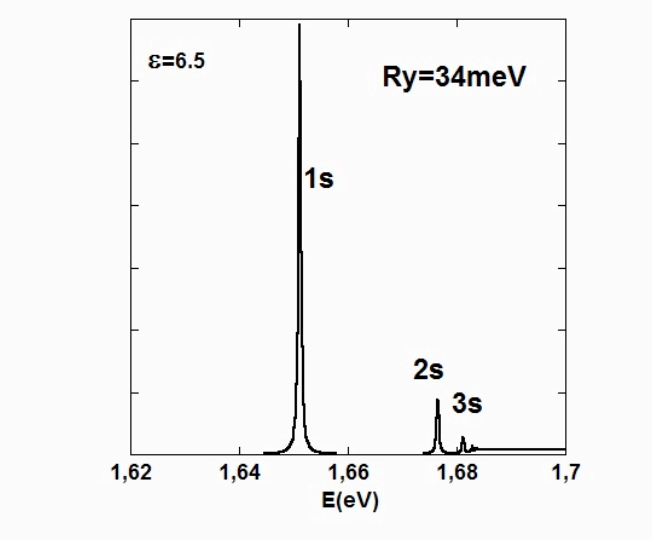

Figure 7.12.

Optical absorption of $CH_3NH_3PbI_3$ computed using the BSE and the exciton Green's function in the linear regime at low temperature. An empirical basis of electron and hole monoelectronic states obtained with the **k.p** method close to the *R* point of the Brillouin zone is used to compute the exciton Green's function. The *e-h* Coulomb interaction is computed with an effective dielectric constant of 6.5. 1s-3s exciton resonances are shown. The electronic band gap is set to 1.685 eV. Reprinted with permission from (Even et al. 2016b).

In the non-linear regime, the BSE equation is strongly modified: *i)* the e-h Coulomb interaction is screened, which is usually represented within the plasmon-pole approximation, *ii)* the oscillator strength is reduced by the phase-space population due to free carriers, *iii)* self-energy contributions for both electrons and holes, lead to band gap renormalization and damping of the exciton resonances.

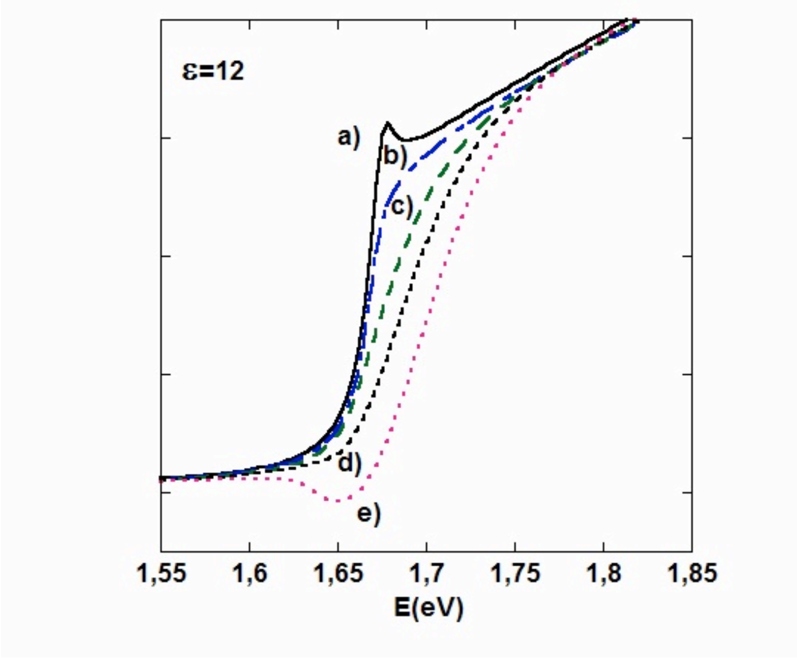

Figure 7.13.

Optical absorption of $CH_3NH_3PbI_3$ computed using the BSE and the exciton Green's function in the non-linear regime at T=160 K. The concentration of free carriers amounts to: a) 0, b) $10^{17}cm^{-3}$, c) $5.10^{17}cm^{-3}$, c) $10^{18}cm^{-3}$, c) $2.10^{18}cm^{-3}$. The band gap in the linear regime is set to 1.685 eV. Reprinted with permission from (Even et al. 2016b).

As illustrated Figure 7.13, for moderate free carrier concentration of about $10^{17}cm^{-3}$, the screening of the exciton resonance is the most important phenomenon. For larger concentrations $5.10^{17}cm^{-3}/10^{18}cm^{-3}$, phase space filling effects start to dominate until population inversion is reached for $2.10^{18}cm^{-3}$. For low carrier concentrations, the band gap renormalization is partially compensated by the screening of the exciton resonance. For large concentration the band gap is shifted to lower values (about 1.65 eV for 2.10^{18}cm^{-3}).

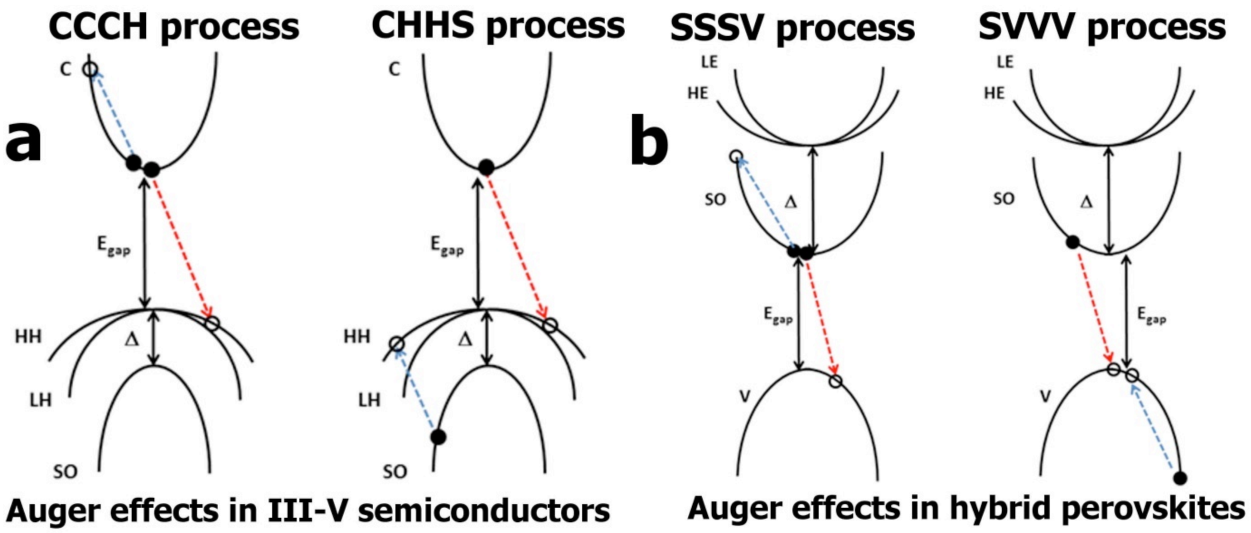

Figure 7.14.

Dominant Auger processes in (a) III-V semiconductors and (b) hybrid perovskites. (a) *HH*, *LH* and *SO* correspond to heavy hole, light hole and hole spin-orbit split-off states of the VB in III-V semiconductors. (b) *HE*, *LE* and *SO* correspond to heavy electron, light electron and electron spin-orbit split-off states of the CB in hybrid perovskites. Reprinted with permission from (Even et al. 2015). Copyright 2015 American Chemical Society.

Light emission close to the band gap is also affected by the presence of large densities of charge carriers in the material. The third-order non-radiative Auger process yields a non-radiative channel in competition with radiative recombination. Before gauging such Auger effects in hybrid perovskites, let us recall what is well known in the field of III-V semiconductors (Figure 7.14(a), (Even et al. 2015)). An electron in the CB may recombine with a heavy hole (*HH*) in the VB, either by transferring energy and momenta to an electronic transition in the CB (*CCCH* or *CHCC* process) or to a hole jumping from the *HH* band to the spin-orbit split-off (SO) band (*CHHS* or *CHSH* process). Among the numerous other possible processes a third *CHLH* or *CHHL* process, not represented here, is usually also considered. This is weaker than the *CHHS* process, except when the spin-orbit splitting energy is larger than the band gap. Since electronic states away from the band gap are involved, the full simulation requires repeated summations over the particle momenta and a careful description of the electronic band structure. The dependence on the electronic band gap, effective masses and carrier densities can be estimated using parabolic approximations for the electronic dispersions:

$$R_{Auger,CCCH} \propto n^2 p e^{-(E_T - E_{gap})/kT} , \tag{7.11}$$

$$R_{Auger,CHHS} \propto n p^2 e^{-(E_T - E_{gap})/kT} , \tag{7.12}$$

where

$$E_{T,CCCH} = \frac{2m_C + m_{HH}}{m_C + m_{HH}} E_{gap} , \tag{7.13}$$

$$E_{T,CHHS} = \frac{2m_{HH} + m_C}{2m_{HH} + m_C - m_{SO}} \left(E_{gap} - \Delta\right) . \tag{7.14}$$

In III-V semiconductors, the Auger effect decreases exponentially as the band gap increases. Moreover, when SOC and the band gap are of the same order of magnitude, the *CHHS* process prevails in most cases. However, in n-type III-V semiconductors, the *CCCH* process is dominant through the $n^2 p$ term. For large band gap materials like GaAs, where Auger processes are very weak, phonon-assisted Auger processes (not described here) give the most important contribution.

The electronic band structure of hybrid perovskites has two important differences with respect to that of III-V semiconductors: *i)* the band structure shows reverse band ordering, with SOC on CB, and *ii)* the effect of SOC is significantly larger than that occuring in III-V semiconductors. Based on the method developed for III-V semiconductors, we can investigate the two most important Auger processes occurring in hybrid perovskites as follows (Figure 7.14(b), (Even et al. 2015)):

$$R_{Auger,SSSV} \propto n^2 p e^{-(E_T - E_{gap})/kT} \qquad (7.15)$$

$$R_{Auger,SVVV} \propto n p^2 e^{-(E_T - E_{gap})/kT} \qquad (7.16),$$

where

$$E_{T,SSSV} = \frac{2m_S + m_V}{m_S + m_V} E_{gap}, \qquad (7.16)$$

$$E_{T,SVVV} = \frac{2m_V + m_S}{m_S + m_V} E_{gap}. \qquad (7.17)$$

An electron in the split-off state (*S*) of CB may recombine with a hole (*V*) in the VB, either by transferring energy and momenta to an electronic transition in the split-off state of the CB (*SSSV* process) or to a hole in the valence band (*SVVV* process). Using effective masses of 0.12 and 0.15 for the split-off CB and for the VB, respectively, we deduce that the *SVVV* process slightly dominates over the *SSSV* process, especially when considering the natural p-doping of hybrid perovskites. However, the overall effect is expected to be small, like in large band gap III-V semiconductors such as GaAs. A process involving the SOC, and heavy electrons (*HE*) or light electrons (*LE*) in the CB (*HSSV* or *LSSV* processes), would require a more detailed analysis, since *HE* and *LE* electronic states lying at high energy in the CB are hybridized with molecular states.

References

(Bernardi et al. 2014) Bernardi, M., D. Vigil-Fowler, J. Lischner, J. B. Neaton, S. G. Louie. 2014. *Phys. Rev. Lett.* 112, 257402-5.

(Billing and Lemmerer 2007) Billing, D. G., and A. Lemmerer. 2007. Synthesis, characterization and phase transitions in the inorganic–organic layered perovskite-type hybrids $[(C_nH_{2n+1}NH_3)_2PbI_4]$, n = 4, 5 and 6. *Acta Cryst. B* 63,735–747.

(Brivio et al., 2014) Brivio, F., K. T. Butler, A. Walsh, M. van Schilfgaarde. 2014. Relativistic quasiparticle self-consistent electronic structure of hybrid halide perovskite photovoltaic absorbers. *Phys. Rev. B* 89:155204.

(Cannuccia and Marini 2011) Cannuccia, E., and A. Marini. 2011. Effect of the Quantum Zero-Point Atomic Motion on the Optical and Electronic Properties of Diamond and Trans-Polyacetylene. *Phys. Rev. Lett.* 107, 255501.

(Cannuccia and Marini 2013) Cannuccia, E., and A. Marini. 2013. Ab-initio study of the effects induced by the electron-phonon scattering in carbon based nanostructures. arXiv:1304.0072 [cond-mat.mtrl-sci].

(Even et al. 2012) Even, J., L. Pedesseau, M.-A. Dupertuis, J.-M. Jancu, C. Katan. 2012. Electronic model for self-assembled hybrid organic/perovskite semiconductors: Reverse band edge electronic states ordering and spin-orbit coupling. *Phys. Rev. B* 86:205301.

(Even et al. 2013) Even, J., L. Pedesseau, J.-M. Jancu, C. Katan. 2013. Importance of spin–orbit coupling in hybrid organic/inorganic perovskites for photovoltaic applications. *J. Phys. Chem. Lett.* 4, 2999-3005.

(Even et al. 2014) Even, J., L. Pedesseau, C. Katan. 2014. Analysis of multi-valley and multi-bandgap absorption and enhancement of free carriers related to exciton screening in hybrid perovskites. *J. Phys. Chem. C* 118:11566– 11572.

(Even et al. 2014b) Even, J., L. Pedesseau, and C. Katan. 2014. Understanding Quantum Confinement of Charge Carriers in Layered 2D Hybrid Perovskites. *ChemPhysChem* 15, 3733-3741.

(Even et al. 2014c) Even, J., L. Pedesseau, J.-M. Jancu, C. Katan. 2014. DFT and k • p modelling of the phase transitions of lead and tin halide perovskites for photovoltaic cells. *Phys. Status Solidi RRL* 8, 31–35.

(Even 2015) Even, J. 2015. Pedestrian Guide to Symmetry Properties of the Reference Cubic Structure of 3D All-Inorganic and Hybrid Perovskites. *J. Phys. Chem. Lett.* 6, 2238-2242.

(Even et al. 2015) Even, J., L. Pedesseau, C. Katan, M. Kepenekian, J.-S. Lauret, D. Sapori, E. Deleporte. 2015. Solid-state physics perspective on hybrid perovskite semiconductors. *J. Phys. Chem. C* 119, 10161-10177.

(Even et al. 2016) Even J., M. Carignano, and C. Katan. 2016. Molecular disorder and translation/rotation coupling in the plastic crystal phase of hybrid perovskites. *Nanoscale* 8, 6222-6236.

(Even et al. 2016b) Even J., Boyer-Richard S., Carignano M., Pedesseau L., Jancu, J.-M., and Katan C. 2016. Theoretical insights into hybrid perovskites for photovoltaic applications. *Proc.*

SPIE 9742, Physics and Simulation of Optoelectronic Devices XXIV, 97421A.

(Fang et al., 2015) Fang, H.-H.; Raissa, R.; Abdu-Aguye, M.; Adjokatse, S.; Blake, G.R.; Even, J.; Loi, M. A. 2015. Photophysics of Organic–Inorganic Hybrid Lead Iodide Perovskite Single Crystals, *Adv. Func. Mat.* 25, 2378–2385.

(Giannozzi et al. 2009) Giannozzi, P., S. Baroni, N. Bonini, M. Calandra, R. Car, C. Cavazzoni, D. Ceresoli, G. L. Chiarotti, M. Cococcioni, I. Dabo, A. Dal Corso, S. de Gironcoli, S. Fabris, G. Fratesi, R. Gebauer, U. Gerstmann, C. Gougoussis, A. Kokalj, M. Lazzeri, L. Martin-Samos, N. Marzari, F. Mauri, R. Mazzarello, S. Paolini, A. Pasquarello, L. Paulatto, C. Sbraccia, S. Scandolo, G. Sclauzero, A. P. Seitsonen, A. Smogunov, P. Umari, R. M. Wentzcovitch. 2009. Ab-initio study of the effects induced by the electron-phonon scattering in carbon based nanostructures *J. Phys.: Condens. Matter* 21, 395502-19.

(Giorgi et al. 2014) Giorgi, G., J.-I. Fujisawa, H. Segawa, K. Yamashita. 2014. Small Photocarrier Effective Masses Featuring Ambipolar Transport in Methylammonium Lead Iodide Perovskite: A Density Functional Analysis. *J. Phys. Chem. C* 118, 12176– 12183.

(Haug and Koch 2009) Haug, H., and S. W. Koch. 2009. *Quantum Theory of the Optical and Electronic Properties of Semiconductors (5th ed.).* New Jersey: World Scientific.

(Hirasawa et al. 1994) Hirasawa, M., T. Ishihara, T. Goto, K. Uchida, and N. Miura. 1994.Magnetoabsorption of the lowest exciton in perovskite-type compound $(CH_3NH_3)PbI_3$. *Physica B.* 201:427-430.

(Ishihara et al. 1990) Ishihara, T., J. Takahashi, T. Goto. 1990. Optical properties due to electronic transitions in two-dimensional semiconductors $(C_nH_{2n+1}NH_3)_2PbI4$. *Phys. Rev.* B 42, 11099-11107.

(Huang and Lambrecht 2013) Huang, L., and W. R. L. Lambrecht, W. R. L. 2013. Electronic band structure, phonons, and exciton binding energies of halide perovskites $CsSnCl_3$, $CsSnBr_3$, and $CsSnI_3$. *Phys. Rev. B* 88, 165203-12.

(Ishihara 1994) Ishihara, T. 1994. Optical properties of PbI-based perovskite structures. *J. Luminescence* 60, 269-274.

(Kato et al. 2003) Kato, Y., D. Ichii, K. Ohashi, H. Kunugita, K. Ema, K. Tanaka,T. Takahashi, and T. Kondo. 2003. Extremely large binding energy of biexcitons in an organic–inorganic quantum-well material $(C_4H_9NH_3)_2PbBr_4$. *Solid State Comm.* 128:15-18.

(Kawai et al. 2014) Kawai, H., K. Yamashita, E. Cannuccia, and A. Marini. 2014. Electron-electron and electron-phonon correlation effects on the finite-temperature electronic and optical properties of zinc-blende GaN. *Phys. Rev. B* 89, 085202.

(Kawai et al. 2015) Kawai, K., G. Giorgi, A. Marini, K. Yamashita. 2015. The Mechanism of Slow Hot-Hole Cooling in Lead-Iodide Perovskite: First-Principles Calculation on Carrier Lifetime from Electron–Phonon Interaction. *Nano Lett.* 15, 3103–3108.

(Koutselas et al. 1996) Koutselas, B., L. Ducasse, and G. C. Papavassiliou. 1996. Electronic properties of three- and low-dimensional semiconducting materials with Pb halide and Sn halide units. *J. Phys. Condens. Matter*. 8, 1217-1227.

(Lautenschlager et al. 1986) Lautenschlager, P., P. Allen, M. Cardona. 1986. Phonon-induced lifetime broadenings of electronic states and critical points in Si and Ge. *Phys. Rev. B* 33, 5501–5511.

(Marini 2008) Marini, A. 2008. *Ab Initio* Finite-Temperature Excitons. *Phys. Rev. Lett*. 101, 06405.

(Marini et al. 2009) Marini, A.; Hogan, C.; Grüning, M.; Varsano, D. 2009. yambo: An ab initio tool for excited state calculations. *Comput. Phys. Commun*. 180, 1392– 1403.

(Mitzi et al. 1995) Mitzi, D.B., S. Wang, C. A. Field, C.A. Chess, and A. M. Guloy. 1995. Conducting layered organic-inorganic halides containing< 110>-oriented perovskite sheets. *Science* 267, 1473-1476.

(Mitzi et al. 2001) Mitzi, D. B., K. Chondroudis, and C. R. Kagan. 2001. Organic-inorganic electronics. *IBM J. Res. Dev.* 2001, 45:29-46.

(Mosconi et al. 2013) Mosconi, E., A. Amat, Md. K. Nazeeruddin, M. Grätzel, F. De Angelis. 2013. First-Principles Modeling of Mixed Halide Organometal Perovskites for Photovoltaic Applications. *J. Phys. Chem. C* 117, 13902–13913.

(Muljarov et al. 1995) Muljarov, E. A., S. G. Tikhodeev, N.A. Gippius, T. Ishihara. 1995. Excitons in self-organized semiconductor/insulator superlattices: PbI-based perovskite compounds. *Phys. Rev. B* 51, 14370-14378.

(Papavassiliou 1997) Papavassiliou, G.C. 1997. Three-and low-dimensional inorganic semiconductors. *Prog. Solid State Chem.* 25, 125–270.

(Pedesseau et al. 2014) Pedesseau, L., J.-M. Jancu, A. Rolland, E. Deleporte, C. Katan, and J. Even. 2014. Electronic properties of 2D and 3D hybrid organic/inorganic perovskites for optoelectronic and photovoltaic applications. *Opt. Quant. Electron.* 46, 1225-1232.

(Restrepo et al. 2009) Restrepo, O. D., K. Varga, S. T. Pantelides. 2009. First-principles calculations of electron mobilities in silicon: Phonon and Coulomb scattering. *Appl. Phys. Lett.* 94, 212103-3.

(Sapori et al. 2016) Sapori, D., M. Kepenekian, L. Pedesseau, C. Katan, and J. Even. 2016. Quantum confinement and dielectric profiles of colloidal nanoplatelets of halide inorganic and hybrid organic–inorganic perovskites. *Nanoscale* 8, 6369-6378.

(Shimizu et al. 2006) Shimizu, M., J. Fujisawa, T. Ishihara. 2006. Photoluminescence of the inorganic-organic layered semiconductor $(C_6H_5C_2H_4NH_3)_2PbI_4$: Observation of triexciton formation. 2006. *Phys. Rev. B* 74, 155206.

(Umari et al. 2014) Umari, P., E. Mosconi, and F. De Angelis. 2014. Relativistic GW calculations on $CH_3NH_3PbI_3$ and $CH_3NH_3SnI_3$ Perovskites for Solar Cell Applications. *Sci. Rep.* 4:4467.

(Xing et al. 2013) Xing, G., N. Mathews, S. Sun, S. S. Lim, Y. M. Lam, M. Grätzel, S. Mhaisalkar, and T. C. Sum. 2013. Long-Range Balanced Electron- and Hole-Transport Lengths in Organic-Inorganic $CH_3NH_3PbI_3$. *Science* 342, 344-347.